ARTICLE　　　　　　　　　　　　　　　　　　　　　　　　　**Open Access**

High energy density of BaTiO₃@TiO₂ nanosheet/ polymer composites via ping-pong-like electron area scattering and interface engineering

Gang Jian [1], Yong Jiao[1], Liang Feng[1], Qingzhen Meng[1], Ning Yang[1], Shangtao Zhu[1], Minfeng Lü [1] and Ching-Ping Wong [2]

Abstract

Dielectric substances exhibit great potential for high-power capacitors due to their high stability and fast charge–discharge; however, a long-term challenge is to enhance energy density. Here, we propose a poly(vinylidene fluoride) (PVDF) composite utilizing BaTiO₃ nanoparticle@TiO₂ nanosheet (BT@TO ns) 2D nanohybrids as fillers, aiming at combining the interfacial strategy of using a core–shell filler and the electron scattering of a 2D filler to improve the energy density. With 4 wt% filler, the composite possesses the largest breakdown strength (E_b) of 561.2 MV m^{-1}, which is significantly enhanced from the 407.6 MV m^{-1} of PVDF, and permittivity of 12.6 at 1 kHz, which is a 23% increase from that of PVDF. A superhigh energy density of 21.3 J cm^{-3} with an efficiency of 61% is obtained at 550 MV m^{-1}. The 2D BT@TO ns-filled composite exhibits a higher energy density than composites filled with core–shell 1D BT@TO nws or non-core–shell 0D BT, 1D TO, or 2D TO particles. The E_b and energy density improvements are attributed to the buffer layer-based interface engineering and enhanced area scattering of electrons caused by the 2D hybrids, an effect similar to that of a ping-pong paddle to scatter electric field-induced charge migrations in composites. Thus, an effective hybrid strategy is presented for achieving high-performance polymer composites that can be used in energy storage devices.

Introduction

As the gradual exhaustion of fossil fuels has become an increasingly thorny problem, international societies have reached a consensus on the exploitation of renewable resources. However, many renewables, such as wind, sun, and tides, rely heavily on electric storage technologies due to their intermittent nature. Electrostatic capacitors are the most environmentally friendly and the longest utilized among all kinds of energy storage devices; thus, they have received increased attention in recent years. In addition, electrostatic capacitors exhibit potential in many areas, such as electric/hybrid vehicles, portable consumer electronics, and electronic weapons due to their pulsed power outputs[1–4]. With continuous efforts to miniaturize and reduce the weights of these devices, a dielectric substance possessing a large energy density and small energy loss is in great demand. The energy density, U, is described as $U = \int E dD$[5–7], where E and D are the electric field and electric displacement, respectively. Notably, linear dielectrics can be described by a simpler expression, i.e., $U = 1/2\varepsilon_0\varepsilon_r E_b$[8], where ε_0, ε_r, and E_b are the free space permittivity and the dielectric constant and breakdown strength of the material, respectively. Apparently, ε_r and E_b are significant parameters for achieving a high energy density, while different kinds of dielectric materials exhibit varied parameters[9]. Polymer–matrix composites that incorporate ceramic fillers have gained considerable attention due to the feasibility of energy density

Correspondence: Gang Jian (gjian@just.edu.cn) or Ching-Ping Wong (cp.wong@mse.gatech.edu)
¹School of Materials Science and Engineering, Jiangsu University of Science and Technology, Zhenjiang 212100, China
²School of Materials Science and Engineering, Georgia Institute of Technology, Atlanta, GA 30332, USA

regulations by tailoring components and loadings in composites[10–12].

In polymer/ceramic composites, E_b normally decreases from that of the polymer matrix because more polymer-ceramic interfaces are generated inside composites, which exist in an unstable state with the accumulation of interfacial space charges; thus, they have higher probabilities of triggering breakdown[2,10,13]. To overcome polymer–ceramic interface problems, various methods have been invented, including polymer additive coatings[14–17], filler surface ionization treatment[18,19], buffer layers[20–23], and in situ polymerization of host polymers[24,25]. Compared to other methods of modifying and optimizing the interface structures by increasing the compatibility between the polymer phases and ceramic particles, the buffer layer method modulates the dielectric constant difference between the polymer matrix and ceramic nanofillers to decrease the intrinsic interfacial charges. Interfacial charges can be high when two phases differ greatly in ε_r[26]. To address such issues, an interfacial engineering strategy has been proposed by researchers and proven to be effective; an ε_r intermediate between those of the polymer and the ceramic is found when utilizing a buffer layer. After coating with an oxide layer, such as Al_2O_3[20], TiO_2 (TO)[21,22], and SiO_2[23], to confine the original interfacial charges inside the core-shell structure, an increase in the E_b of the composite occurs. Lin and coworkers demonstrated that $BaTiO_3$ (BT)@TO hybrid nanofibers exhibited enhanced energy density due to the confinement of interfacial charges[22]. Bi and coworkers showed that $BT@SiO_2$ hybrid fillers exhibited an enhanced E_b and energy density (11.5 J cm^{-3}, 64%) from those of neat polymers and polymeric composites incorporating BT particles[23]. Oxide coating layers (~5–48) are linear dielectrics with ε_r values larger than that of the polymeric matrix (~2–10) and lower than ferroelectric core particles (~2000–3300) at 1 kHz[27–29]; additionally, they are highly insulative.

For such core–shell strategies, an effective buffer substance is only constructed in the area near the ceramic particles, which cannot cut the electric tree paths in matrices. However, highly insulating platelet-like fillers can enhance the E_b of the polymer matrix by the electron scattering effect. Polymer composites filled with hBN (ε_r ~3–5) or mica nanosheets (nss) give rise to an increased E_b[30–32]. Notably, electron scattering is highly influenced by filler morphology, i.e., 0D nanoparticles (nps) and 1D nanowires (nws)/nanofibers (nfs), show much less scattering than 2D nss do. The present studies on interfacial engineering of 0D or 1D hybrids still provide limited E_b values. The paradox is that hBN nss may not be a promising candidate as a buffer layer between ferroelectric particles and polymers to effectively reduce interfacial charges because it has a low ε_r, lower than those of some polymers. Hence, the design of appropriate nanofiller structures to effectively utilize electron scattering and maintain interfacial engineering is necessary for the development of polymer composites with a superhigh energy density.

In this work, we propose a poly(vinylidene fluoride) (PVDF) composite incorporated with BT@TO ns nanofillers. High-quality TO nss and BT nps are presynthesized by hydrothermal and sol-gel methods, respectively, and then hybrids are prepared through filtration-stacking and heat treatment. The TO shell (ε_r ~48) provides several benefits, i.e., it is a buffer substance between PVDF and BT (due to $\varepsilon_{BT} > \varepsilon_{TO} > \varepsilon_{PVDF}$) to decrease and confine interfacial charges and as a large-area insulating platelet to scatter electrons in the polymer. Our work reveals that an enhanced E_b (~561.2 MV m^{-1}), discharged energy density (U_d ~21.3 J cm^{-3}), and charge–discharge efficiency (η ~61%) are achieved in the PVDF/BT@TO ns-4 wt% composite, which shows the effectiveness of significantly improving the energy storage performance in composites via the combination of interfacial engineering and electron scattering and indicates the high potential for the use of composites in high power energy storage devices.

Materials and methods
Synthesis of TO nss, BT nps, and BT np@TO ns hybrid particles

TO nss with lateral sizes of ~300–400 nm and an average thickness of ~5 nm were synthesized via the hydrothermal approach: 20 mL of tetrabutyl titanate (Ti($C_{16}H_{36}O_4$), 98%, Aladdin, China) was mixed with 9 mL of 48 wt% hydrofluoric acid solution and 10 mL of ethanol with stirring for 1.5 h. The solution was loaded into a 100 mL stainless steel polytetrafluoroethylene-lined autoclave. The synthesis was performed at 180 °C for 16 h. The reaction product particles were rinsed with deionized water, collected via a vacuum filtration process, and dried at 85 °C for 2 h in air.

Fine BT nps with a size of approximately 40 nm were synthesized via the sol-gel approach. Barium acetate (0.05 mol, Ba($C_4H_6O_4$), 99%, Aladdin, China), and tetrabutyl titanate (0.05 mol) were dissolved in 33.5 mL of deionized water and in a solution containing 12 mL of acetic acid and 36 mL of ethanol, respectively. Then, the Ba solution was transferred and stirred slowly into the Ti solution within 15 min to trigger the hydrolysis reaction. The reaction was continuously stirred for 12–24 h, causing the sol to transition into a gel. BT np powders were obtained after drying the gel and calcining at 700 °C in the air for 2–3 h.

Presynthesized BT np and TO ns powders at a volume ratio of 1:3 were mixed by adding ethanol and stirring for 2 h and ultrasonicating for 2 h. Vacuum filtration was

employed to obtain stack-structured particles on filter paper. The hybrid structures were heat-treated at 450 °C in the air for 3–4 h to form BT@TO ns hybrids.

Preparation of dielectric films

Two grams of PVDF were dissolved into 12 g of N-methylpyrrolidone (NMP, Aladdin, China) in a closed glass container by stirring for 24 h or ultrasonicating for 12 h. BT@TO ns hybrid powders with loadings of 2–8 wt% to the PVDF composites were added to the PVDF solution, which was then ultrasonicated for 12 h. The water in the sonicating bath was changed every 30 min to keep it at a low temperature. Films were coated onto glasses, cured at 120 °C for 8 h in air, and then at 170 °C for 8 min in air. After that, the films were immersed in cold water, peeled off from the substrate, and dried at 65 °C for 2 h. The PVDF films and PVDF composites filled with TO nws (FT-3000, ISK Ltd., Japan, the scanning electron microscopy (SEM) image is presented in Fig. S1), and BT nps were prepared through a similar procedure. The composite and polymer films were prepared with a thickness of approximately 20 µm. The silver paste was screen printed onto the films to prepare electrodes with a bottom-side area of ~25 mm^2 and a top side consisting of several ~1 mm^2 dots.

Characterization

SEM measurements were carried out by using a Quanta FEG 250 instrument at a 20 kV acceleration voltage. High-resolution transmission electron microscopy (HRTEM) micrographs were taken by using a JEM-2100F instrument at a 200 kV acceleration voltage. Energy dispersive X-ray (EDX) spectroscopy mapping was measured by using a Noran spectrometer on the JEM-2100F instrument. Atomic force microscopy (AFM) micrographs and height profiles were taken by using an NT-MDT NTE-GRA instrument. X-ray diffraction (XRD) patterns were obtained with a PANalytical B.V. diffractometer. X-ray photoelectron spectroscopy (XPS) was carried out by using a Thermo Scientific Nexsa XPS system. Fourier transform infrared (FTIR) spectroscopy was performed with a Mettler Toledo ReactIR 45 instrument. The breakdown tests were carried out by utilizing a direct current breakdown instrument (Nanjing Changsheng CS2674AX) with a 20,000 V voltage limit. Dielectric parameters were measured by using an Agilent 4294A impedance analyzer. D–E loops were measured (100 Hz, room temperature) by using the aixACCT TF Analyzer 2000E tester with a TREK P0621P high-voltage amplifier with a 30,000 V voltage limit.
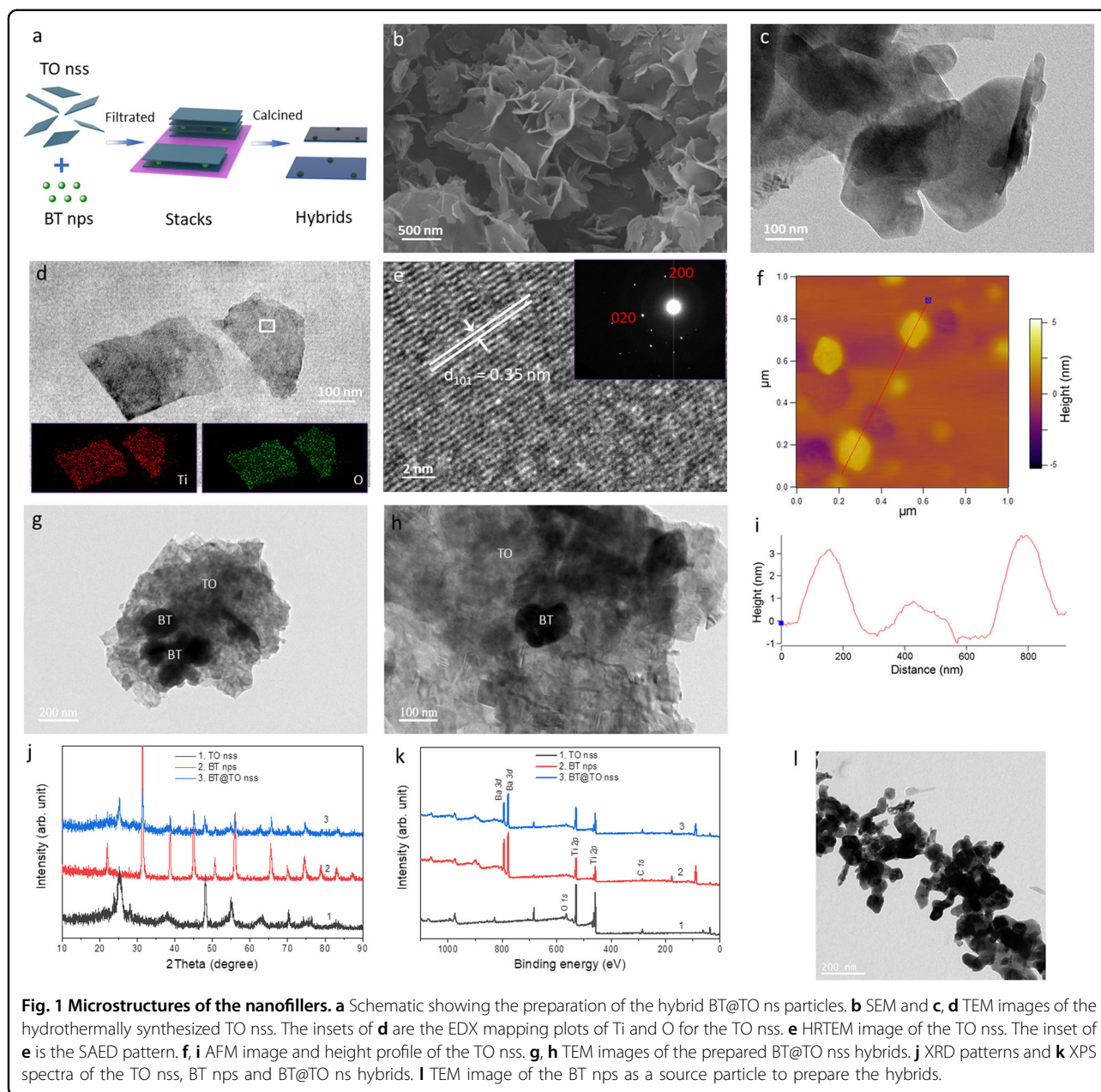
Simulation

The finite-element simulation was performed with the Comsol Multiphysics platform by constructing a material model with dimensions of 5 µm (length) × 4 µm (width) × 3 µm (height). The voltage at the top edge was 1500 V, and that at the bottom edge was 0 V. The permittivities (2000, 48, and 10.2 for BT, TO, and PVDF, respectively) and electrical conductivities (10^{-11}, 10^{-14}, and 10^{-15} S/m for BT, TO, and PVDF, respectively) of the material components were fitted in the model. Solutions were obtained through calculations for the numerical results of interfacial charge, displacement and electric current flows in the composite.

Results and discussion

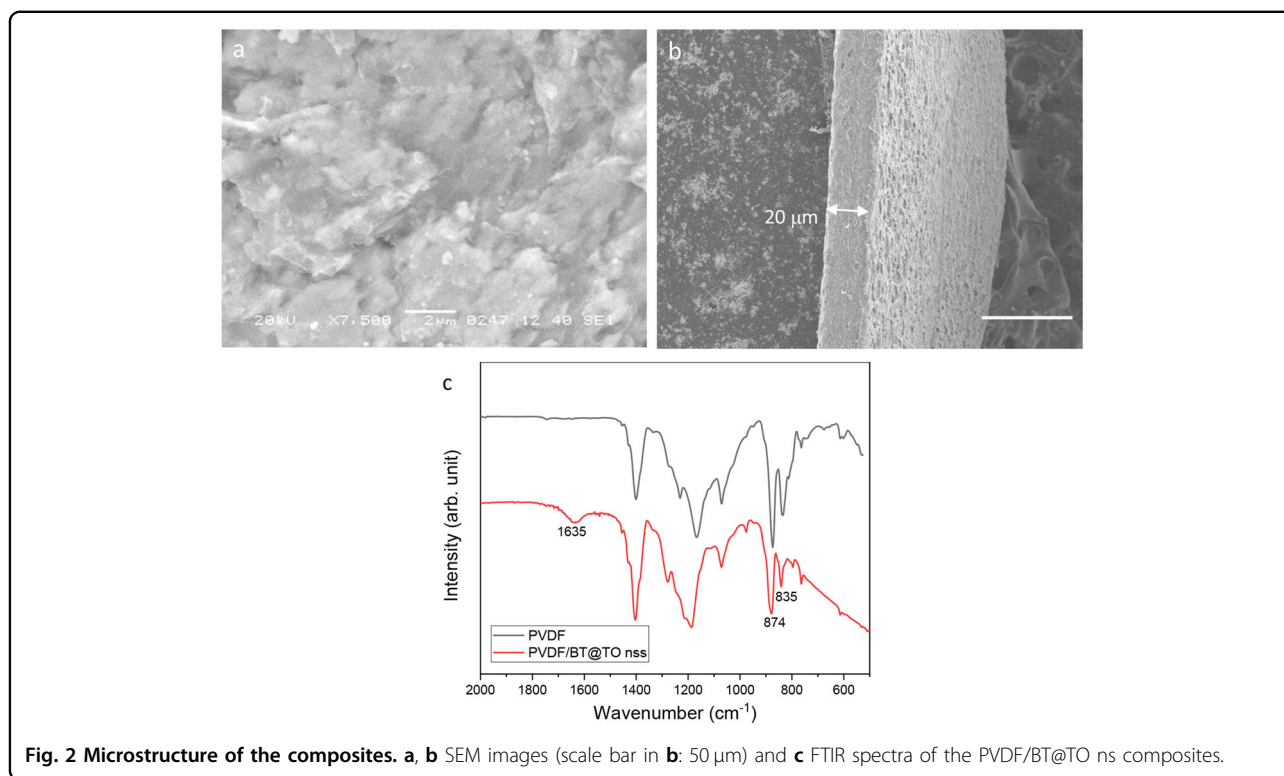### Microstructures of the nanofillers and dielectric film

Figure 1a shows a schematic for the preparation of BT@TO ns hybrids via a filtration-stacking and heat-treatment process. The BT@TO ns hybrid consists of two or more thin, large-area TO nss acting as the host/covering layer and several BT nps acting as the core particles. The stacked hybrid structure is formed at the filtration-stacking step, while the tight binding of BT–TO is formed after the heat treatment, which is accompanied by mass transfer. Figure 1b–d shows the SEM and TEM images of the TO nss synthesized via the hydrothermal approach. A superthin nanosheet morphology is observed, with thicknesses of 3–5 nm and lateral sizes of 300–400 nm; thus, these nss have a very large area/thickness aspect ratio of ~100–150. The function of hydrofluoric acid in the hydrothermal reaction is to expose the (001) face of TO, leading to the formation of a 2D nanosheet morphology, and the function of ethanol is to work as an auxiliary modifier to further increase the (001) exposure and to promote the formation of superthin nss with a layer thickness of 2–3 atoms[33]. The EDX mappings in the insets of Fig. 1d indicate that Ti and O are present. From the HRTEM image in Fig. 1e, a lattice spacing of 0.35 nm corresponds to the (101) plane, indicating the anatase structure of TiO_2, which is also in accordance with the XRD results. Figure 1e also indicates the excellent homogeneity of the TO nss. The selected area electron diffraction pattern in the inset of Fig. 1e can be indexed as the [001] zone axis diffraction, indicating that the TO nss are well crystallized and that the surfaces of the TO nss are {001} facets[34]. The AFM image and the corresponding height profile in Fig. 1f, i demonstrate the nanosheet morphology of the TO nss and the thickness of 3–4 nm of the TO nss, respectively. BT nps with a spherical shape and a uniform size of approximately 40 nm (Fig. 1l and Fig. S2) are obtained via the sol–gel approach described in our previous work[35]. The diameter of the BT nps is smaller than the lateral size of the TO nss for forming hybrid coverings. Figure 1e, f shows the TEM images of the BT@TO nss. The hybrid reveals a sheet-like morphology (lateral sizes of 500–600 nm and thickness of 10–15 nm), which indicates that the TO nss are apt to

Fig. 1 Microstructures of the nanofillers. a Schematic showing the preparation of the hybrid BT@TO ns particles. **b** SEM and **c, d** TEM images of the hydrothermally synthesized TO nss. The insets of **d** are the EDX mapping plots of Ti and O for the TO nss. **e** HRTEM image of the TO nss. The inset of **e** is the SAED pattern. **f, i** AFM image and height profile of the TO nss. **g, h** TEM images of the prepared BT@TO nss hybrids. **j** XRD patterns and **k** XPS spectra of the TO nss, BT nps and BT@TO ns hybrids. **l** TEM image of the BT nps as a source particle to prepare the hybrids.

form orderly sheet-stacking structures rather than erected or curled structures. Several BT nps are embedded in the TO nss to achieve a core–shell type structure, as observed in the images, which indicates the successful formation of the designed BT@TO ns structure.

Figure 1j shows the XRD patterns of the synthesized TO nss, BT nps and BT@TO hybrids. The TO nss and BT nps belong to the anatase TO phase (JCPDS no. 21-1272, $a = 3.785$ Å, $c = 9.513$ Å, space group $I4_1/amd$)[36] and a cubic BT phase (JCPDS no. 31-0174, $a = 4.031$ Å, space group Pm3m)[37], respectively. The BT@TO ns hybrids are confirmed to have two phases (BT nps and TO nss). Outside of those of the BT nps and TO nss phases, no

miscellaneous peaks are observed in the pattern of the hybrids, which indicates that there are no chemical phase reactions. The composition of the BT@TO ns hybrids can also be confirmed by XPS measurements. The existence of Ba and Ti in the BT@TO hybrids is confirmed by the complete XPS spectra in Fig. 1k. The binding energy peak position of an element depends on the oxidation state and local chemical environment of that element[38]. The high-resolution binding spectra in Fig. S3 show that the Ti *2p* and Ba *3d* peaks of the BT@TO hybrids shift positively from those of the BT nps and negatively from the Ti *2p* of the TO nss. This is because the local chemical environment of those elements changes in the hybrids, which is

Fig. 2 Microstructure of the composites. a, **b** SEM images (scale bar in **b**: 50 µm) and **c** FTIR spectra of the PVDF/BT@TO ns composites.

indicative of a rather strong coupling and good contact between BT and TO in the hybrids[39]. Therefore, the XPS results indicate that the BT nps do not float on the TO nss surface in the BT@TO hybrids but are inserted between the TO nss and demonstrate tight binding. The large strain that exists in the interface region is also favorable for the enhanced polarization of the composites[22].

Figure 2a, b shows the SEM images of the PVDF/BT@TO ns composites prepared by solution casting. As observed, the film is dense and neat without any pores or voids. Moreover, no apparent filler aggregation is found, which indicates that composite films are uniform in microstructure, while fillers are well dispersed. Figure 2c shows the FTIR spectra of PVDF and its composite. Characteristic peaks at 874 and 835 cm^{-1} indicate that PVDF is fully polymerized and forms a β-phase[40]. In the pattern of the PVDF/BT@TO ns composite, in addition to the characteristic peaks of PVDF, a peak at ~1635 cm^{-1} is due to the BT@TO hybrids[41,42].

Dielectric behavior of the composites

Figure 3 shows the frequency-dependent dielectric constant and the loss tangent of the PVDF/BT@TO ns composites (100–5 MHz) at room temperature. The ε_r of the composite continuously increases with increasing BT@TO ns loading, indicating that the introduction of BT@TO nss effectively enhances the ε_r of the matrix due to the high k of BT and the TO buffer layer present

Fig. 3 Dielectric properties of the composites. Frequency-dependent ε_r and tanδ of the PVDF/BT@TO ns composites at room temperature.
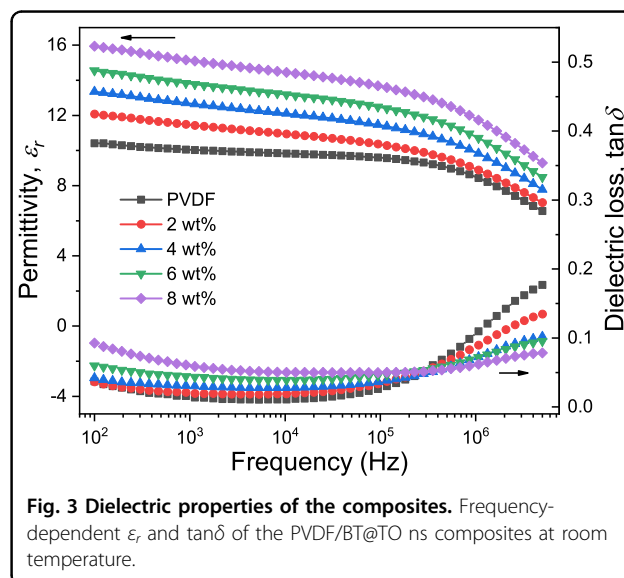
between BT and PVDF[43]. The ε_r values at 1 kHz of the PVDF/BT@TO ns composites with filler loadings of 2, 4, 6, and 8 wt% are 11.4, 12.6, 13.7, and 15.1, respectively. Comparatively, this value is 10.2 for neat PVDF at 1 kHz. All materials with various filler loadings reveal a low dissipation of approximately 0.02 at 1 kHz. This low conduction loss is the main reason for the low dielectric loss.
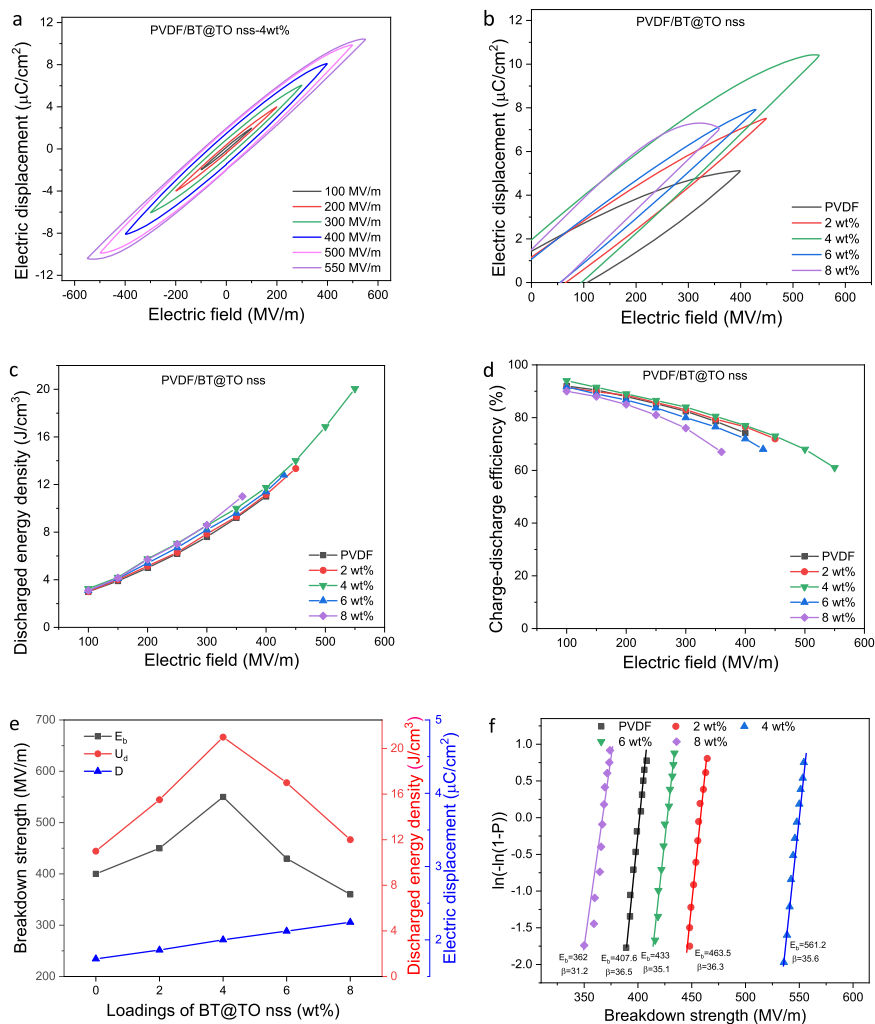
Fig. 4 Energy storage performance of the 2D hybrid filler-based PVDF composites. a D–E hysteresis loops of the PVDF/BT@TO ns-4 wt% composite in various electric fields. **b** D–E hysteresis loops of the PVDF/BT@TO ns composites at different filler loadings. **c** Electric-field dependent U_d of the PVDF/BT@TO ns composites. **d** Electric-field dependent η of the PVDF/BT@TO ns composites. **e** E_b, D, and U_d at 100 MV m^{-1} changing with the BT@TO ns loading. **f** Weibull distribution of the PVDF/BT@TO ns composites at different filler loadings.

Energy storage performance of the composites

Figure 4a shows the D–E loops of the PVDF/BT@TO ns-4 wt% composite in various external electric fields. Higher displacement is achieved in a higher electric field because more polarization is generated. All hysteresis loops present narrow shapes, which indicates that the PVDF/BT@TO ns-4 wt% composite has a relatively small energy loss. The loop exhibits a trend toward flattening with increasing electric field due to the electrically resistive nature of the films. At 100 and 550 MV m^{-1}, the displacements of the composite are 1.8 and 9.15 μC cm^{-2}, respectively.

Figure 4b shows the D–E loops of the PVDF/BT@TO ns composites containing various amounts of fillers. When the BT@TO ns concentration is increased from 0 wt% (i.e., neat PVDF) to 8 wt%, the displacements of the

PVDF/BT@TO ns composites in a specific electric field increase accordingly. The PVDF/BT@TO ns composites show narrowed loops compared with those of neat PVDF, indicating an improvement in energy efficiency and a decrease in the energy loss of the composites. Regarding the PVDF/BT@TO ns composite-8 wt%, the loop flattens, indicating an increase in energy loss. The largest displacement among all different materials is found for the PVDF/BT@TO ns-4 wt% composite, indicating that an optimal filler loading exists to achieve the best energy storage performance. The maximum displacements of the PVDF/BT@TO ns composites with filler loadings of 0, 2, 4, 6, and 8 wt% are 5.1, 7.5, 9.15, 7.9, and 7.1 μC cm^{-2}, respectively. The PVDF/BT@TO ns-4 wt% composite possesses the largest displacement, which may be due to the high k of BT[44] and the effective transition path from

BT to PVDF ($\varepsilon_{BT} > \varepsilon_{TO} > \varepsilon_{PVDF}$) and the possible high local electric field and high local displacement induced by the BT@TO hybrid particles.

The discharged energy density (U_d) of the composites is obtained from the left curve of the enclosed area of the D–E loops (Fig. 4c). U_d gets larger in a higher electric field. The maximum U_d ($U_{d,\max}$) of composites with various filler loadings differ due to comprehensive variations in the displacement and E_b. Among the materials, the largest $U_{d,\max}$ of 21.3 J cm^{-3} is achieved in the PVDF/BT@TO ns-4 wt% composite at 550 MV m^{-1}, which is approximately 2 times that of 11 J cm^{-3} for neat PVDF at the highest bearable field of 400 MV m^{-1}. When the filler loading is 2 and 8 wt%, the PVDF/BT@TO ns composites possess a $U_{d,\max}$ of 13.35 and 11.05 J cm^{-3}, respectively.

Figure 4d shows the electric field-dependent charge–discharge efficiency (η) of the PVDF/BT@TO ns composites. The PVDF/BT@TO ns-4 wt% composite achieves an η value higher than those of PVDF and of composites with other filler loadings; this is due to its small dielectric loss and high insulative property. At 400 MV m^{-1}, the η of the PVDF/BT@TO ns-4 wt% composite is 77%, which is larger than those of composites containing 2 wt% ($\eta \approx 76\%$) and 6 wt% ($\eta \approx 72\%$) BT@TO nss and neat PVDF ($\eta \approx 74.2\%$). Moreover, η decreases gradually with increasing electric field strength due to the resistive nature of the composites; for instance, at 550 MV m^{-1}, when $U_{d,\max}$ is achieved in the PVDF/BT@TO ns-4 wt% composite, η has a value of 61%, which is high compared with the values in the literature[20–23].

The relationships among the critical parameters that reflect the energy storage properties of the composites after BT@TO loading are analyzed, as shown in Fig. 4e. We find that a high increase in the comprehensive energy storage performance of the composites is induced by a small loading of the BT@TO ns hybrids.

Additionally, the E_b values of the PVDF/BT@TO ns composites are evaluated with a Weibull two-parameter distribution, $\ln[-\ln(1-P)] = -\beta \ln \alpha + \beta \ln E$[45,46], where E is the experimental breakdown field of each test, P is the probability of electrical breakdown among the tests, β indicates the E dispersion and α indicates E where 63.2% of the materials are broken. In Fig. 4f, the values of β for the composites are higher than 30, indicating high reliability with a narrowed data distribution. The highest E_b is 561.2 MV m^{-1} for the PVDF/BT@TO ns-4 wt% composite with a high β value of 35.6, while the E_b of neat PVDF is 407.6 MV m^{-1}. The enhanced E_b of PVDF/BT@TO ns composites may be mainly ascribed to the following aspects: (i) The confinement of space charges within the BT@TO hybrids by the TO layer, which confines the space charges to a more stable state and (ii) the electron scattering effect of the 2D BT@TO nss leads to a decrease in the free charge flow in the composites and blocks the breakdown paths in the polymer.

To investigate the effects of the BT@TO ns hybrids on the displacement behavior of the composites, the D–E loops at 100 MV m^{-1} of PVDF and the various composites, e.g., PVDF/TO nss, PVDF/TO nws, PVDF/BT nps, and PVDF/BT@TO nss with a 4 wt% filler loading, are presented in Fig. 5a. The electric displacement is important for obtaining a high U_d in a specific electric field, which is 1.5 μC cm^{-2} for PVDF at 100 MV m^{-1}. After the addition of the BT@TO ns hybrids and BT nps, the displacements increase to 2 and 1.75 μC cm^{-2}, respectively. Regarding the TO nss- and TO nws-filled PVDF composites, the displacements are 1.8 and 1.68 μC cm^{-2}, respectively. The difference in the displacement between the PVDF/TO ns and PVDF/TO nw composites is likely caused by variations in the filler connectivity inside the composites.

The E_b values of the four types of composites are shown in Fig. 5b. At a 4 wt% filler loading, enhanced E_b values are observed for composites filled with TO nss, TO nws, and BT@TO ns hybrids compared to that of neat PVDF, indicating that filling with small amounts of such fillers improves the E_b of PVDF. The PVDF/BT np composite possesses the lowest E_b among the investigated materials due to the low insulating nature of BT. Among the four composites, PVDF/BT@TO nss and PVDF/TO nss achieve the highest improvement in E_b. More importantly, choosing different TO fillers leads to obviously different results, i.e., a higher E_b is achieved with PVDF/TO nss (505.3 MV m^{-1}) than with PVDF/TO nws (433 MV m^{-1}). This is due to the improved electron scattering from the large-area platelet-like fillers.

Figure 5c shows the $U_{d,\max}$ of PVDF and the four types of composites. At a filler loading of 4 wt%, the four types of fillers show enhanced $U_{d,\max}$ compared with neat PVDF. The PVDF/BT np composite shows a $U_{d,\max}$ similar to that of PVDF. Moreover, a higher $U_{d,\max}$ is achieved with the PVDF/TO nw composite. A high $U_{d,\max}$ is achieved with PVDF/TO nss due to the high E_b. The largest $U_{d,\max}$ is then achieved with the PVDF/BT@TO ns composites due to simultaneous high E_b and high displacement.

In comparison, the published properties of the PVDF-TrFE-CFE/BN nss[30], PVDF/ZrO$_2$ nss[47], PVDF/BT@Al$_2$O$_3$ nfs[20], PVDF/BT@TO nfs[21,22], and PVDF/BT@SiO$_2$[23] composites are discussed. The highest E_b and η are all found in nanosheet-incorporated composites, which indicates the effective scattering of free charges caused by 2D fillers. The highest E_b of 600 MV m^{-1} is achieved with PVDF-TrFE-CFE/BN nss. This is also attributed to the E_b of 565 MV m^{-1} of the PVDF-TrFE-CFE matrix, which is high among polymers. Our work achieves the highest $U_{d,\max}$ with the BT@TO ns-filled PVDF composites,
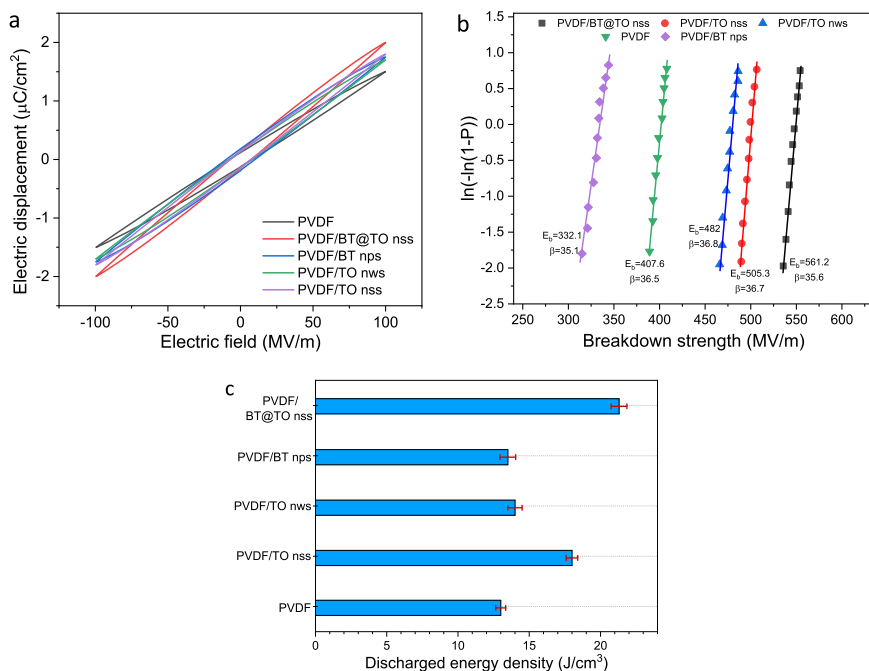
Fig. 5 Comparison of the dielectric and energy storage performance. a D–E hysteresis loops of PVDF and the various composites (PVDF/TO nss, PVDF/TO nws, PVDF/BT nps, and PVDF/BT@TO nss) with a 4 wt% filler loading at 100 MV m^{-1}. **b** Weibull distribution of PVDF and the various composites (PVDF/TO nss, PVDF/TO nws, PVDF/BT nps, and PVDF/BT@TO nss) at 4 wt% filler loading. **c** U_d of PVDF and the various composites at 4 wt% filler loading.
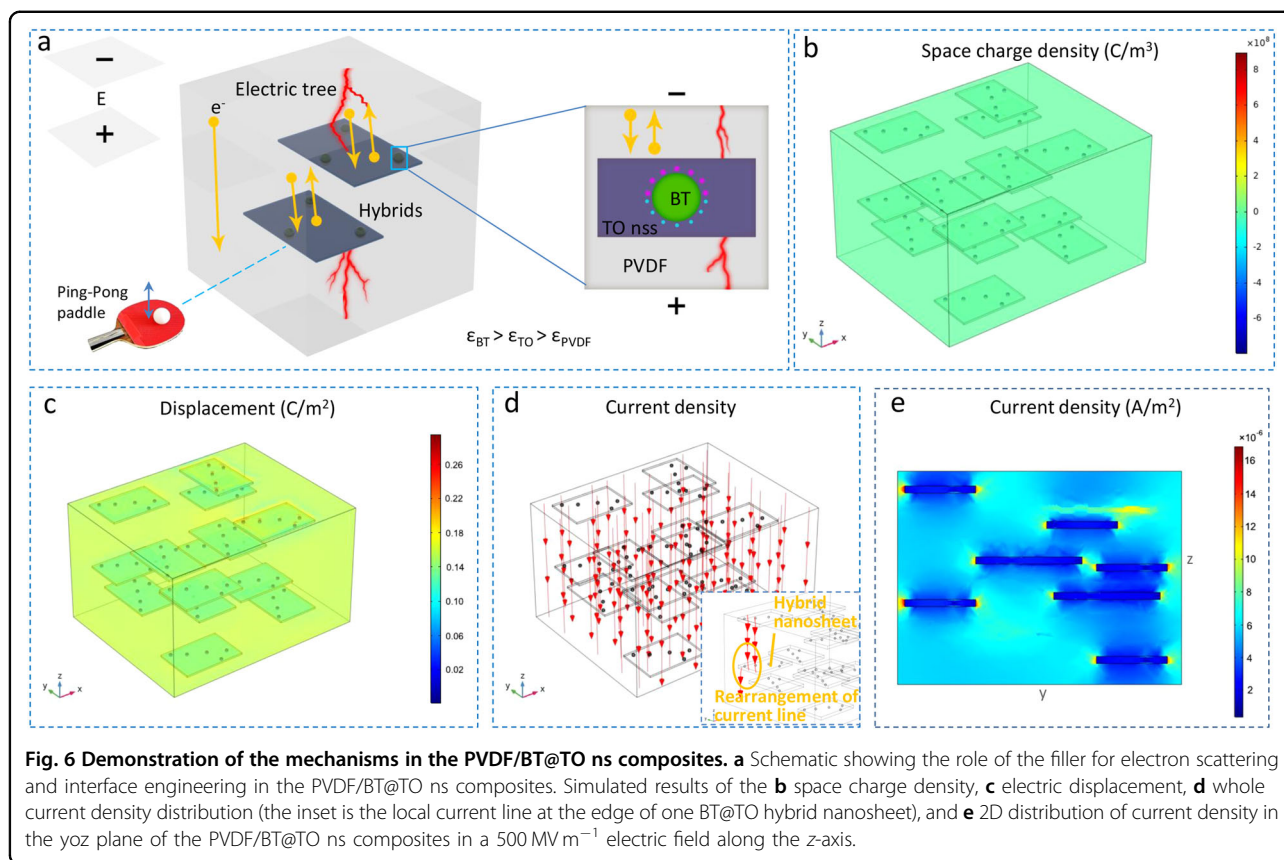
which stems from the synergistic improvement in the E_b and displacement and indicates that the BT@TO ns hybrid structure is a more effective way of improving energy storage performance.

Mechanism of the 2D BT@TO ns-filled PVDF composites

As an aid to comprehension, the mechanism for the improvement in E_b and U_d of the PVDF/BT@TO ns composites is shown in Fig. 6a. The figure includes the following aspects: (i) the highly insulating BT@TO nss with a 2D morphology enables the effective scattering of electrons in polymers; simultaneously, the BT@TO nss can block the breakdown electric tree in the composites. In composites where no BT@TO nss are locally blocked, free-electron flow exists. Regarding the effect of filler morphology on electron scattering, it can be understood that it is much easier to hit a ping-pong ball with a ping-pong paddle (2D) than to hit a baseball with a baseball bat (1D). In the PVDF/BT@TO ns composites, the elastic scattering of electrons caused by 2D hybrids largely reduces the free migration of charges in composites in external electric fields, therefore improving their E_b. (ii) TO acts as a buffer between PVDF and BT ($\varepsilon_{BT} > \varepsilon_{TO} > \varepsilon_{PVDF}$), which confines space charges at the interfaces and effectively transfers the dielectric constant and displacement from the high k BT to PVDF, thus enhancing the parameters of the composites. Regarding

the relationship between the buffer layer and electron scattering, the buffer layer function is related to the material properties of TO, while electron scattering is mainly related to the 2D shapes of TO. Due to the existing function of the TO buffer layer, namely, decreasing the difference in the dielectric constant between BT and PVDF, for tetragonal BT with a higher degree of ferroelectricity, the energy storage property of the composites will not change much. The electron scattering effect may also not be influenced by the BT phases in the hybrids.

Finite element analysis of the PVDF/BT@TO ns composites was performed to explore the energy storage mechanism. The dielectric constant ratios of BT/PVDF and TO/PVDF are set to 200 and 4.6, respectively, in the simulation model. An external electric field of 500 MV m^{-1} along the z-axis is adopted. The simulated results in Fig. 6b show that space charges are concentrated at the BT–TO interface rather than at the TO–PVDF interface due to the higher ε_r difference between BT and TO than that between TO and PVDF[26], indicating the excellent interfacial charge confinement of the highly insulative TO layer. From Fig. 6c, it can be observed that very high simulated local displacement of up to ~28 μC cm^{-2} exists at the BT–TO interfaces due to a local electric field effect[11,22], which enables the enhanced displacement in composites (experimental data ~9 μC cm^{-2}) by the hybrid filler structure. Figure 6d shows that the basic current

Fig. 6 Demonstration of the mechanisms in the PVDF/BT@TO ns composites. a Schematic showing the role of the filler for electron scattering and interface engineering in the PVDF/BT@TO ns composites. Simulated results of the **b** space charge density, **c** electric displacement, **d** whole current density distribution (the inset is the local current line at the edge of one BT@TO hybrid nanosheet), and **e** 2D distribution of current density in the yoz plane of the PVDF/BT@TO ns composites in a 500 MV m^{-1} electric field along the *z*-axis.

flow line is from the top to the bottom, which indicates the many possible scatterings of the BT@TO nss. The detailed current line simulation in the inset of Fig. 6d at the edge of the BT@TO hybrid nanosheet indicates that the current line passing by a nanosheet is rearranged (two lines → one line). The rearrangement of current lines can also be observed in Fig. S4, as current lines are bent when passing by the hybrids. The current line rearrangement illustrates the function of the BT@TO nss toward influencing the initial migrations of electrons in the composites. The 2D model current density simulation in Fig. 6e shows that along the path in which the 2D BT@TO hybrid filler exists, the electric current is small compared with that in paths without the 2D hybrids, illustrating the function of the nanosheet to scatter electrons in the composites. The direct result of this blocking is to increase the breakdown strength of the composite from the neat polymer matrix[30].

It should be noted that filling with the BT@TO nss still introduces interface defects in the composites; on the other hand, the filler can comprehensively improve the E_b of the matrix. Therefore, optimal filler loading should be sought until the balance is reached. Due to the existing function of the TO buffer layer for decreasing the difference in the dielectric constant between BT and PVDF, regarding tetragonal BT with its higher degree of

ferroelectricity, the energy storage property of the composites will not fluctuate much. The electron scattering effect may also not be influenced by the BT phases in the hybrids. Because the preparation of hybrids and composites is facile, economical, and highly repeatable, the approach reported here shows great possibilities for application to real industrial products. This strategy should also be applicable to multilayer-structured dielectric substances.

Conclusion

In summary, the BT@TO ns 2D hybrid particles with high aspect ratios and their polymer–matrix composites are presented in this work, aiming at combining the advantages of interfacial engineering for core–shell fillers and electron scattering for 2D platelet fillers to achieve an effective improvement in the energy density of the composites. The optimal PVDF/BT@TO ns-4 wt% composite reveals a dielectric constant of 12.6 and a loss of 0.021 at 1 kHz. The composite also possesses a high E_b of ~561.2 MV m^{-1}, which is a large increase from the 407.6 MV m^{-1} of neat PVDF. The resulting $U_{d,max}$ of ~21.3 J cm^{-3} with η of ~61% is realized with the composite at 550 MV m^{-1}. The existence of an optimal filler loading for achieving the maximum energy density is due to the balance between the interface defects introduced by

the BT@TO nss and the improvement in the E_b of the matrix by the filler. The 2D BT@TO ns-filled composite exhibits a higher energy density than composites filled with core-shell 1D BT@TO nws or non-core–shell 0D BT, 1D TO, or 2D TO particles. The enhanced E_b may stem from two aspects: (i) the effective buffer function of the TO shell between PVDF and BT ($\varepsilon_{BT} > \varepsilon_{TO} > \varepsilon_{PVDF}$), which decreases the space charge at interfaces, and (ii) the enhanced area of electron scattering is caused by the 2D BT@TO nss, which blocks and reduces the direct migration of free charges across the composites when in an electric field. Finite element simulation reveals that the current flow lines are rearranged through the 2D fillers and that the values are lower. This study presents a significant and facile hybrid strategy to develop polymer-–matrix composites with excellent performance for application in high-power electrostatic capacitors.

Author contributions
G.J. and C.P.W. conceived the idea, designed the experiments, and analyzed the data. G.J. wrote the paper. Y.J. prepared the materials and performed the electrical measurements. L.F. and Q.M. did the simulation. N.Y., S.Z., and M.L. analyzed the data. C.P.W. supervised the experiments. All authors discussed the results and contributed to the paper.

Conflict of interest
The authors declare that they have no conflict of interest.

Publisher's note
Springer Nature remains neutral with regard to jurisdictional claims in published maps and institutional affiliations.

Supplementary information The online version contains supplementary material available at https://doi.org/10.1038/s41427-022-00356-w.

References
1. Huang, X. & Jiang, P. Core-shell structured high-k polymer nanocomposites for energy storage and dielectric applications. *Adv. Mater.* **27**, 546–554 (2015).
2. Luo, S. et al. Significantly enhanced electrostatic energy storage performance of flexible polymer composites by introducing highly insulating-ferroelectric microhybrids as fillers. *Adv. Energy Mater.* **9**, 1–8 (2019).
3. Pan, H. et al. Ultrahigh-energy density lead-free dielectric films via polymorphic nanodomain design. *Science* **365**, 578–582 (2019).
4. Luo, N. et al. Constructing phase boundary in AgNO₃ antiferroelectrics: pathway simultaneously achieving high energy density and efficiency. *Nat. Commun.* **11**, 4824 (2020).
5. Wang, Y. et al. Design strategy of barium titanate/polyvinylidene fluoride-based nanocomposite films for high energy storage. *J. Mater. Chem. A* **8**, 884–917 (2020).
6. Chu, B. et al. A dielectric polymer with high electric energy density and fast discharge speed. *Science* **313**, 334–336 (2006).
7. Li, J., Zhang, L. & Ducharme, S. Electric energy density of dielectric nanocomposites. *Appl. Phys. Lett.* **90**, 132901 (2007).
8. Dang, Z., Yuan, J., Yao, S. & Liao, R. Flexible nanodielectric materials with high permittivity for power energy storage. *Adv. Mater.* **25**, 6334–6365 (2013).
9. Luo, H. et al. Interface design for high energy density polymer nanocomposites. *Chem. Soc. Rev.* **48**, 4424–4465 (2019).
10. Zhang, X. et al. Superior energy storage performances of polymer nanocomposites via modification of filler/polymer interfaces. *Adv. Mater.* **5**, 1800096 (2018).
11. Jian, G. et al. Enhanced dielectric constant and energy density in a BaTiO3/polymer-matrix composite sponge. *Commun. Mater.* **1**, 91 (2020).
12. Jian, G. et al. Hydrothermal synthesis of BaTiO3 nanowires for high energy density nanocomposite capacitors. *J. Mater. Sci.* **55**, 6903–6914 (2020).
13. Wang, Y. et al. Significantly enhanced breakdown strength and energy density in sandwich-structured barium titanate/poly(vinylidene fluoride) nanocomposites. *Adv. Mater.* **27**, 6658–6663 (2015).
14. Guo, N. et al. Supported metallocene catalysis for in situ synthesis of high energy density metal oxide nanocomposites. *J. Am. Chem. Soc.* **129**, 766–767 (2007).
15. Yang, K., Huang, X., Huang, Y., Xie, L. & Jiang, P. Fluoro-Polymer@BaTiO3 hybrid nanoparticles prepared via RAFT polymerization: toward ferroelectric polymer nanocomposites with high dielectric constant and low dielectric loss for energy storage application. *Chem. Mater.* **25**, 2327–2338 (2013).
16. Luo, H. et al. Improved dielectric properties and energy storage density of poly(vinylidene fluoride-co-hexafluoropropylene) nanocomposite with hydantoin epoxy resin coated BaTiO3. *ACS Appl. Mater. Interfaces* **7**, 8061–8069 (2015).
17. Pan, Z., Yao, L., Zhai, J., Yao, X. & Chen, H. Interfacial coupling effect in organic/inorganic nanocomposites with high energy density. *Adv. Mater.* **30**, e1705662 (2018).
18. Zhou, T. et al. Improving dielectric properties of BaTiO3/ferroelectric polymer composites by employing surface hydroxylated BaTiO3 nanoparticles. *ACS Appl. Mater. Interfaces* **3**, 2184–2188 (2011).
19. Kim, P. et al. Phosphonic acid-modified barium titanate polymer nanocomposites with high permittivity and dielectric strength. *Adv. Mater.* **19**, 1001–1005 (2007).
20. Pan, Z. et al. Excellent energy density of polymer nanocomposites containing BaTiO3@Al2O3 nanofibers induced by moderate interfacial area. *J. Mater. Chem. A* **4**, 13259–13264 (2016).
21. Rahimabady, M., Mirshekarloo, M. S., Yao, K. & Lu, L. Dielectric behaviors and high energy storage density of nanocomposites with core-shell BaTiO3@TiO2 in poly(vinylidene fluoride-hexafluoropropylene). *Phys. Chem. Chem. Phys.* **15**, 16242–16248 (2013).
22. Zhang, X. et al. Ultrahigh energy density of polymer nanocomposites containing BaTiO3/TiO2 nanofibers by atomic-scale interface engineering. *Adv. Mater.* **27**, 819–824 (2015).
23. Bi, K. et al. Ultrafine core-shell BaTiO3@SiO2 structures for nanocomposite capacitors with high energy density. *Nano Energy* **51**, 513–523 (2018).
24. Zhang, T. et al. Modulating interfacial charge distribution and compatibility boosts high energy density and discharge efficiency of polymer nanocomposites. *RSC Adv.* **9**, 3599–35997 (2019).
25. Zha, J., Dang, Z., Zhou, T., Song, H. & Chen, G. Electrical properties of TiO2-filled polyimide nanocomposite films prepared via an in situ polymerization process. *Synth. Met.* **160**, 2670–2674 (2010).
26. Ducharme, S. An inside-out approach to storing electrostatic energy. *ACS Nano* **3**, 2447–2450 (2009).
27. Pan, Z., Zhai, J. & Shen, B. Multilayer hierarchical interfaces with high energy density in polymer nanocomposites composed of BaTiO3@TiO2@Al2O3 nanofibers. *J. Mater. Chem. A* **5**, 15217–15226 (2017).
28. Xu, J. et al. Enhanced energy density of PVDF-based nanocomposites via a core-shell strategy. *Sci. Rep.* **10**, 17084 (2020).
29. Prateek, Thakur, V. K. & Gupta, R. K. Recent progress on ferroelectric polymer-based nanocomposites for high energy density capacitors: synthesis, dielectric properties, and future aspects. *Chem. Rev.* **116**, 4260–4317 (2016).
30. Li, Q. et al. Solution-processed ferroelectric terpolymer nanocomposites with high breakdown strength and energy density utilizing boron nitride nanosheets. *Energy Environ. Sci.* **8**, 922–931 (2015).
31. Zhu, Y. et al. High energy density polymer dielectrics interlayered by assembled boron nitride nanosheets. *Adv. Energy Mater.* **9**, 1901826 (2019).
32. Wu, L. et al. Improved breakdown strength of poly(vinylidene fluoride)-based composites by using all ball-milled hexagonal boron nitride sheets without centrifugation. *Compos. Sci. Technol.* **190**, 108046 (2020).

33. Li, M. et al. Ultrathin anatase TiO2 nanosheets for high-performance photo-catalytic hydrogen production. *Small* **13**, 1604115 (2017).

34. Yang, L. et al. Tuning the photoelectronic and photocatalytic properties of single-crystalline TiO_2 nanosheet array films with dominant {001} facets by controlling the hydrochloric acid concentration. *J. Mater. Sci.* **51**, 950–957 (2016).

35. Jian, G. et al. Microstructure and multiferroic properties of $BaTiO_3$/$CoFe_2O_4$ films on Al_2O_3/Pt substrates fabricated by electrophoretic deposition. *J. Eur. Ceram. Soc.* **33**, 1155–1163 (2013).

36. Gu, L., Wang, J., Cheng, H., Du, Y. & Han, X. Synthesis of nano-sized anatase TiO2 with reactive {001} facets using lamellar protonated titanate as precursor. *Chem. Commun.* **48**, 6978–6980 (2012).

37. Ni, Q., Zhu, Y., Yu, L. & Fu, Y. One-dimensional carbon nanotube@barium titanate@polyaniline multiheterostructures for microwave absorbing applica-tion. *Nanoscale Res. Lett.* **10**, 174 (2015).

38. Wagner, C. D. et al (Ed.) *Handbook of X-ray Photoelectron Spectroscopy.* (Perkin-Elmer Corp., MN, 1979).

39. Shen, J. et al. Accelerating photocatalytic hydrogen evolution and pollutant degradation by coupling organic co-catalysts with TiO2. *Chin. J. Catal.* **40**, 380–389 (2019).

40. Kim, P. et al. High energy density nanocomposites based on surface-modified BaTiO3 and a ferroelectric polymer. *ACS Nano* **3**, 2581–2592 (2009).

41. Tang, H., Lin, Y. & Sodano, H. A. Synthesis of high aspect ratio BaTiO3 nano-wires for high energy density nanocomposite capacitors. *Adv. Energy Mater.* **3**, 451–456 (2013).

42. Yao, P., Zhong, S. & Shen, Z. TiO2/halloysite composites codoped with carbon and nitrogen from melamine and their enhanced solar-light-driven photo-catalytic performance. *Int. J. Photoenergy* **5**, 1–8 (2015).

43. Prateek, Bhunia, R., Siddiqui, S., Garg, A. & Gupta, R. K. Significantly enhanced energy density by tailoring the interface in hierarchically structured TiO_2-$BaTiO_3$-TiO_2 nanofillers in PVDF-based thin-film polymer nanocomposites. *ACS Appl. Mater. Interfaces* **11**, 14329–14339 (2019).

44. Jian, G. et al. A strategy for design of non-percolative composites with stable giant dielectric constants and high energy densities. *Nano Energy* **58**, 419–426 (2019).

45. Zhang, X. et al. Achieving high energy density in PVDF-based polymer blends: suppression of rarely polarization saturation and enhancement of breakdown strength. *ACS Appl. Mater. Interfaces* **8**, 27236–27242 (2016).

46. Danikas, M. G. & Tanaka, T. Nanocomposites—a review of electrical treeing and breakdown. *IEEE Electr. Insul. Mag.* **25**, 0883–7554 (2009).

47. Shen, Y. et al. Enhanced breakdown strength and suppressed leakage current of polyvinylidene fluoride nanocomposites by two-dimensional ZrO_2 nanosheets. *Mater. Express* **6**, 277–282 (2016).